Draft: Orthogonal Decomposition Analysis and Optimization of Turbine Vane Endwall Horseshoe Vortex Dynamics and Heat Transfer

Markus Schwänen[*] **and Andrew Duggleby**
Department of Mechanical Engineering
Texas A&M University
College Station, TX 77843

Paul Fischer
Mathematics and Computer Science Division
Argonne National Laboratory
Argonne, IL 60439

The stagnating boundary layer vortex, also known as the horseshoe vortex, on a gas turbine endwall is investigated by using direct numerical simulation. This vortex is disruptive to the protective cooling layer because it drives hot combustion gases to the endwall surface. It exhibits significant dynamical motions that further increase the surface heat transfer. The dynamics of the horseshoe vortex must be characterized in a 3D time-resolved fashion in order to better understand their impact on heat transfer augmentation. In this paper, a first-stage high-pressure stator passage is examined by using spectral-element direct numerical simulation at a Reynolds number $Re=U_\infty C/\nu = 10,000$. Although this is lower than engine conditions, the vortex exhibits similar strong, aperiodic motions. A novel inflow generation technique is introduced to generate appropriate initial conditions, which are challenging especially for gas turbine engine flows that are characterized by high free-stream turbulence and large, integral-length scales. The inflow consists of a periodic solution of Taylor vortices that are convected over a square grid. The size of the vortices and grid spacing is used to control the integral-length scale, and the intensity of the vortices and upstream distance between the grid and vane is used to control the turbulence intensity. The vortex system is analyzed by using a time correlation-based orthogonal decomposition. The resulting basis functions are ranked with respect to their contribution to the turbulent heat flux. The endwall is then shaped to enhance the modes that reduce heat transfer, resulting in a lower overall heat transfer in the stagnation region.

Nomenclature

$A_i(\vec{x},t)$	Signal vector containing nondimensional velocity and temperature
C	Chord
C_{ax}	Axial chord
DNS	Direct numerical simulation
Ec	Eckert number
POD	Proper orthogonal decomposition
$\dot{q}_W$	Specific wall heat flux
Re	Reynolds number $\mathrm{Re} = \frac{U_\infty C}{\nu}$
St	Stanton number $St = \frac{h}{\rho c_p U_\infty}$
T	Static temperature
$\mathfrak{T}$	Nondimensionalized and weighted temperature
$\overline{T_{in}}$	Average inflow temperature
$\overline{T_{out}}$	Average exit temperature
U_∞	Freestream velocity
X,Y,Z	Streamwise, pitchwise, and spanwise coordinate
α^k	Eigenvalue of mode k
Λ	Integral-length scale
$\varphi^k(\vec{x})$	Scalar spatial basis function of mode k
$\Psi_i^k(t)$	Time basis function of mode k and index i
ν	Molecular viscosity

1 Introduction

Gas turbine engines are responsible for a considerable part of the world's electricity generation and most aviation transport. Even though the burning of fossil fuel has become more expensive, the gas turbine will continue to play a significant role in energy conversion and propulsion. Despite decades of advances, the gas turbine remains one of the most complex systems ever built, with many aspects that are still

———
[*]Corresponding author. Email: markus.schwaenen@gmx.net

not fully understood. This situation translates into a large potential for performance and efficiency increase.

With regard to the thermal-fluid aspects of the gas turbine, highly resolved spatial and temporal measurements of fluid velocity and temperature are needed to further unravel the complex physics. Specifically in gas turbine endwall cooling, turbulent convection is dominated by secondary flow structures originating from the blade geometry. One example is the stagnating boundary-layer vortex, depicted in Fig. 1, left, which exhibits high spatial oscillations in addition to its large mean swirl. This vortex is responsible for a large amount of drag and part failure due to melting, depicted in Fig. 1, right.

Experimental investigations have given some insight into the physics associated with the horseshoe vortex. Gaugler and Russell [1] studied the stagnating boundary-layer vortex flow in turbomachinery in a time-resolved manner. Through flow visualization and surface heat transfer, they showed that high convective heat transfer coincides with the most intense vortex action. Laser doppler velocimetry measurements in the stagnation region of a first-stage turbine stator vane were performed by Kang et al. [2]. The contours of turbulent kinetic energy indicate a peak in the turbulent kinetic energy at the location of the horseshoe vortex center. Streamwise, lateral, and vertical root-mean-square velocity profiles show that the location of these peak values coincide closely with the center of the vortex. Only the peak streamwise fluctuations occur slightly upstream of the vortex center. The fluctuations are much higher in the vortex region than in a canonical turbulent boundary layer. Similarly high levels were shown previously by Devenport and Simpson [3]. The unsteady motion of the horseshoe vortex is believed to account for the increased turbulence measured. Radomsky and Thole [4] presented histograms of the probability density functions that show two distinct peaks near the endwall, particularly in the vortex center. These indicate that the flow is oscillating or unsteady. The high turbulence intensities in combination with the unsteady vortex and wall-generated turbulence greatly enhance the endwall heat transfer [4]. Effects of high freestream turbulence intensities on the endwall region were further studied by Gregory-Smith and Cleak [5]. The results showed that the mean flow field is not greatly affected by high freestream turbulence and that high turbulence within the blade passage is present near the end wall. Spencer et al. [6] examined flow in an annular cascade of nozzle guide vanes. Using a transient liquid crystal technique to measure heat transfer, they showed that the horseshoe vortex did not create a region of high heat transfer near the leading edge of the hub endwall.

To date, experiments indicate that the effect of a stagnating boundary-layer vortex on gas turbine endwall heat transfer is both time-dependent and highly unsteady. As supercomputing power continues to increase, direct numerical simulation (DNS) of turbulent heat transfer in gas turbines can significantly add to the domain knowledge. Since DNS does not use turbulence modeling, the errors typically associated with the high anisotropy of the flow are not present; and the velocity, pressure, and temperature at every point are
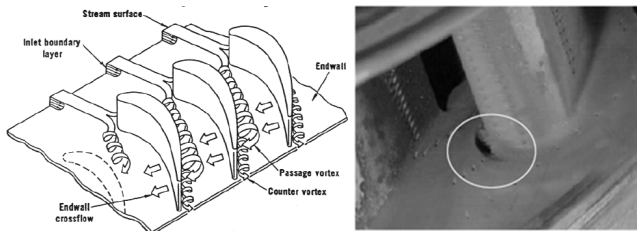

Fig. 1. The horseshoe vortex rolls up from the stagnating boundary, depicted by Langston [7] (left). These secondary flow structures are responsible for melting because they drive hot combustion gases toward the endwall (right, from Thole [8]).

available. However, the computational cost to obtain this data at industrially relevant Reynolds numbers is typically prohibitive. Although once simulated, even at low Reynolds numbers the subsequent data can be analyzed with incredible detail through advanced postprocessing techniques to observe structures, interactions, and correlations, helping to characterize the physics and enable next-generation improvements and modifications. Presented in this paper is the first of such simulations and analysis. Although the Reynolds number examined (10,000) is lower than engine conditions, the vortex already exhibits strong aperiodic motions, and any uncertainty due to subgrid-scale modeling is avoided in the DNS.

As part of this work, a new method of appropriate inlet conditions in the preprocessing stage and a new method of modifications in the postprocessing stage developed at Texas A&M are shown as applied to a gas turbine simulation.

For inlet conditions it is desired to achieve a developing flat plate boundary layer subject to high freestream turbulence intensity and length scale. The two principal ways of generating inlet conditions are described. Sadiki et al. [9] developed a preprocessing technique where inflow data is generated beforehand from user-defined Reynolds stresses. These data files then need to be read into the Navier-Stokes solver during run time, a procedure that makes this method hard to implement preserving parallel efficiency. Jacobs and Durbin [10] have shown a way to describe elevated freestream turbulence at the inlet from Fourier modes that resemble grid turbulence. Even though their inlet conditions are based on some physical insight, the conditions rely on random variables and are not free of divergence. We describe here a new method using what is typically an experimental technique: convecting a flow with subtle fluctuations over a set of physical grids in order to generate and decay grid turbulence to desired values. The new method of postprocessing and endwall modification analyzes the direct numerical simulation's highly resolved spatial and temporal data through proper orthogonal decomposition (POD). In POD the flow is decomposed into orthogonal basis functions. Ball et al. [11] applied POD to data from direct numerical simulation of channel flow in order to understand bursting and sweeping events in the internal turbulent boundary layer. Later, the same methodology was used by Duggleby et al. [12] on a direct numerical simulation of pipe flow. Turbulent structures

in the boundary layer could be linked to certain POD modes and the energy transfer between them better understood. Because of the more complex blade geometry, a direct computation of orthogonal functions from spatial correlations is not efficient. An alternative method was used by Aubry et al. [13], who demonstrated the equivalence of orthogonal basis functions derived from time and space autocorrelations. This time-based method was used by Handler et al. [14] to analyze the properties of turbulent channel flow when creating drag reduction through the use of polymers in the flow. In our study, a time-dependent DNS of a first-stage stator vane and endwall is performed in order to examine the structures and dynamics of the dominant horseshoe vortex and characterize its effect on endwall heat transfer. That structure is then manipulated by endwall contouring, resulting in an overall reduction in heat transfer in the stagnation region.

To recap, this paper presents the first DNS of gas turbine endwall turbulent heat transfer, using "natural" inlet boundary conditions; identifies the main structures responsible for heat transfer; and dampens those structures through endwall contouring. In the next section, the numerical method is presented. This is followed by the simulation results, POD analysis and results, and endwall modification and results.

2 Numerical method

The incompressible Navier-Stokes equations were solved by using a spectral element method (see Fischer et al. [15]). Heat transfer was incorporated by solving the energy equation as a passive scalar and matching the Prandtl number of air. The mesh consists of 94,032 hexahedral elements. Within each, the solution was approximated by seventh order Legendre polynomials. The grid resolution provides a maximum wall distance of the nearest cell on the endwall of $z^+ < 1$. For improved stability, the last two modes of the Legendre polynomials were multiplied with a quadratic filter function such that the last mode was reduced by 5%. Employing spectral elements provides parallel efficiency, accuracy, and exponential convergence. In order to show grid convergence, the total force magnitude on the blade was measured for 50 time steps and different Legendre polynomial order. The solution was always started from the same fully developed field, and force data were averaged over the last 40 steps. The deviation of force magnitude from the highest resolution is plotted as a function of polynomial order and shows a decrease (Fig. 2). Time discretization was done with high-order operator splitting methods, and tensor-product polynomial bases were solved by using conjugate gradient iteration with a scalable Jacobi and hybrid Schwarz/multigrid preconditioner [16]. The time step was chosen such that the Courant number is always below 2. Every 500 time steps, a data sample was saved for later postprocessing. A total of 150 samples was collected, spanning close to 18 flowthroughs based on axial chord and freestream velocity.

A single blade in the cascade with periodic boundary conditions in the pitchwise direction was considered. The bottom spanwise boundary was treated as a no-slip wall,
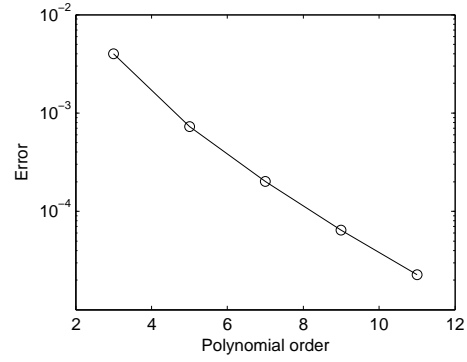

Fig. 2. The error in total force magnitude on the blade is plotted as a function of solution polynomial order or grid resolution. Convergence is obtained. The simulation was run at order 7.
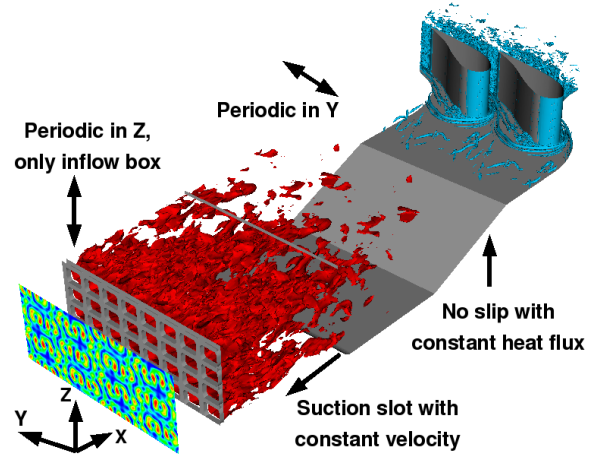

Fig. 3. The flow domain consists of a single blade with periodic boundary conditions in the pitchwise (Y) direction. At the inflow plane, a divergence free vortex field is defined. Grid bars redistribute energy, and the inflow parameters are controlled by geometric features such as ramp slope and length or domain length.

where a constant specific-heat flux was applied from $X/C > -1/3$. The outflow was located 0.75 C downstream (X direction) of the trailing edge. The inflow was placed about 4.60 C upstream of the blade stagnation including the turbulence generating section. A slip condition (stress free) was applied at the top, at half-blade span.

2.1 Numerical domain and boundary conditions

At the inlet, at $X/C = -4.6$, a divergence-free velocity field with multiple vortices is defined as shown by Walsh [17] (see Fig. 3). The streamfunction ψ of the velocity field is given by

$$\psi = \frac{1}{4}\cos(3z)\sin(4y) - \frac{1}{5}\cos(5y) - \frac{1}{5}\sin(5z). \quad (1)$$

Since the streamfunction also obeys $-\nabla^2\psi = \kappa\psi$, where κ is the eigenvalue of the Laplacian, one can control the
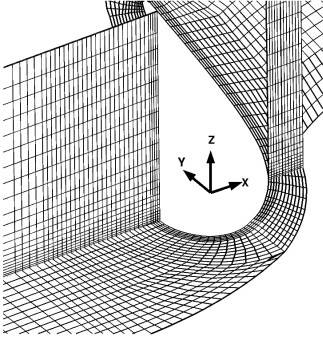
Fig. 4. The element mesh is shown on the stagnation plane (X/Z) and the endwall (X/Y). The mesh is refined near the walls.

freestream turbulence intensity and length scales by varying the amplitude and wavenumbers of the sine and cosine functions, respectively. As long as it is smaller than the open grid area, the average size of these eddies controls the length scale. Smaller vortices can be achieved by increasing the wavenumber. The inflow section was a doubly periodic (in Y and Z) box that extended to $X/C = -3.1$. At $X/C = -4.2$, an array of bars causes the redistribution of turbulent kinetic energy downstream of the inflow plane across all three velocity components. The distance between grid and cascade can be changed during run time and determines the decay rate. In order to maintain elevated levels of turbulence intensity in spite of the low Reynolds number, a forcing term was added to the momentum equation, which artificially decreases viscosity in the region downstream of the bars to the middle of the ramp. The mesh was refined in the wall normal directions around the blade and the endwall (see Fig. 4). Those additional element layers were introduced downstream of the inflow box, connected to it by a backward-facing step. Since preliminary simulations indicated the accumulation of low momentum fluid in the trough, the step was made porous and sucks fluid in the negative x direction. This approach avoids entrainment of low momentum fluid into the main flow when exiting the inflow box. The boundary layer is controlled by a ramp downstream of the step (extending from $X/C = -2$ to $X/C = -1$).

2.2 Time orthogonal decomposition

Following the derivation shown by Aubry et al. [13], an orthogonal decomposition is proposed that yields a scalar spatial function set and a vectorial time function set. Consider $A_i(x,t)$ to be a real, measurable, square-integrable, vectorial function of space and time,

$$A_i(x,t) = [u,v,w,\mathfrak{T}], \mathbf{A} \in L^2(X \times \mathbf{T}), X \subset \mathbb{R}^1, \mathbf{T} \subset \mathbb{R}^4,$$

where u, v, and w are the nondimensionalized velocity components in the streamwise, spanwise, and wall normal direction, respectively. Internal energy is represented by nondimensionalized and weighted temperature as shown in Eq. (2). The Eckert number Ec weights the temperature in

an energy sense.

$$\mathfrak{T}(\vec{x},t) = Ec \frac{T(\vec{x},t) - \overline{T_{in}}}{T_{out} - T_{in}} \tag{2}$$

$$Ec = \frac{U_0^2}{c_v(T_{out} - T_{in})} \tag{3}$$

T_{in} is the averaged domain inflow temperature or freestream temperature, and T_{out} is the area-averaged temperature at the domain outlet. With spectral operator analysis, one can show that the signal can be decomposed into scalar spatial functions $\varphi^k(\vec{x})$ and vector temporal function sets $\Psi_i^k(t)$ for the kth eigenfunction,

$$A_i(\vec{x},t) = \sum_{k=0}^{\infty} \alpha^k \varphi^k(\vec{x}) \Psi_i^k(t). \tag{4}$$

From solving the eigenvalue problem

$$\int_0^{\mathcal{T}} r_{ij}(t,t') \Psi_j^k(t') dt' = (\alpha^k)^2 \Psi_i^k(t) \tag{5}$$

$$r_{ij}(t,t') = \int_X A_j(\vec{x},t) A_i(\vec{x},t') dx, \tag{6}$$

the time basis functions are computed. The spatial integration $\int_X$ is numerically approximated by a summation over all control volumes. The finite cell volumes are known from the meshed geometry. The time integration $\int_0^{\mathcal{T}}$ is approximated by using a trapezoidal quadrature. As described by Ball et al. [11]), the integration weight $w_{(t)}$ needs to be applied in a way to preserve matrix symmetry.

$$r_{ij}(t,t') \Psi_i^k(t') w(t') = (\alpha^k)^2 \Psi_i^k(t) \tag{7}$$

$$\sqrt{w(t')} r_{ij}(t,t') \sqrt{w(t)} \chi_i^k(t') = (\alpha^k)^2 \chi_i^k(t') \tag{8}$$

The eigenproblem solution will provide the new basis functions $\chi_i^k(t) = \Psi_i^k(t) \sqrt{w(t)}$, which need to be transformed back to $\Psi_i^k(t)$ for further analysis.

The spatial eigenfunctions $\varphi^k(\vec{x})$ are obtained from projecting the time function set $\Psi_i^k(t)$ onto the signal

$$\int_0^{\mathcal{T}} A_i(\vec{x},t) \Psi_i^k(t) dt = \alpha^k \varphi^k(\vec{x}). \tag{9}$$

In order to perform a quantitative analysis, all basis functions must be scaled appropriately to yield the correct dimensional field. By combining Eqs. (4) and (9), one arrives at

$$A_i(\vec{x},t) = \sum_{k=0}^{\infty} \int_0^{\mathcal{T}} A_j(\vec{x},t) \Psi_j^k(t) dt \Psi_i^k(t). \tag{10}$$

The orthonormal time basis functions that most numerical eigenproblem solvers deliver can now be used directly without further scaling. The basis functions have some favorable

mathematical properties:

$$\alpha^0 \geq \alpha^1 \geq \ldots > 0$$

$$\lim_{N \to \infty} \alpha^N = 0$$

$$(\varphi^k, \varphi^l) = (\Psi_i^k, \Psi_i^l) = \delta_{kl}.$$

Since the eigenvalues α^k represent the fraction of the global system energy (kinetic and thermal), the decomposition is optimal in that the lowest number of modes is needed to reconstruct a given fraction of the full data set.

To rank each modes relevance to heat transfer, we define a three-dimensional, cubic control volume on a flat surface for which an energy balance based on enthalpy can be written (see Kays and Crawford [18]). In the present study, this control volume is bounded by the endwall, where a constant specific heat flux is imposed as a boundary condition. Since the top is a symmetry plane, there are no fluxes across this boundary. A simplified energy balance is then obtained:

$$\dot{q}_s'' = \frac{\partial}{\partial x} \int_0^{\frac{Z}{2}} \rho u h \, dz + \frac{\partial}{\partial y} \int_0^{\frac{Z}{2}} \rho v h \, dz. \tag{11}$$

The enthalpy $h = c_p(T - T_\infty)$ is defined based on the freestream (inlet) temperature. With Reynolds decomposition and the Gauss divergence theorem, this expression can be evaluated over areas of interest. In this study, the box spans from $X/C = -1/3$ to the vane front, from $Y/P = -0.4$ to $Y/P = 0.4$, and from $Z/S = 0$ to $Z/S = 0.5$.

$$\bar{q}_s = \oint_L \left[\int_0^{\frac{Z}{2}} \rho \bar{u} c_p (\bar{T} - T_\infty) \, dz \right] \vec{e}_x \cdot \vec{n} \, dL$$

$$+ \oint_L \left[\int_0^{\frac{Z}{2}} \rho \bar{v} c_p (\bar{T} - T_\infty) \, dz \right] \vec{e}_y \cdot \vec{n} \, dL$$

$$+ \oint_L \left[\int_0^{\frac{Z}{2}} \rho c_p \overline{u'T'} \, dz \right] \vec{e}_x \cdot \vec{n} \, dL$$

$$+ \oint_L \left[\int_0^{\frac{Z}{2}} \rho c_p \overline{v'T'} \, dz \right] \vec{e}_y \cdot \vec{n} \, dL \tag{12}$$

Orthogonal basis functions are used to evaluate this expression, and the integrals are computed along the lines enclosing the area of interest.

2.3 Deriving an endwall contour

Once an important time orthogonal decomposition mode was identified with the procedure described above, a wall contour based on its spatial information was derived; see Fig. 5, top left. This was achieved by first generating an isosurface based on $\varphi^k(\vec{x})$ (in this study at ± 1.5, with a tolerance of ± 0.4, where the tolerance in effect yields an isosurface thickness). The wall normal coordinates of all grid points within this isovolume and closest to the endwall were then
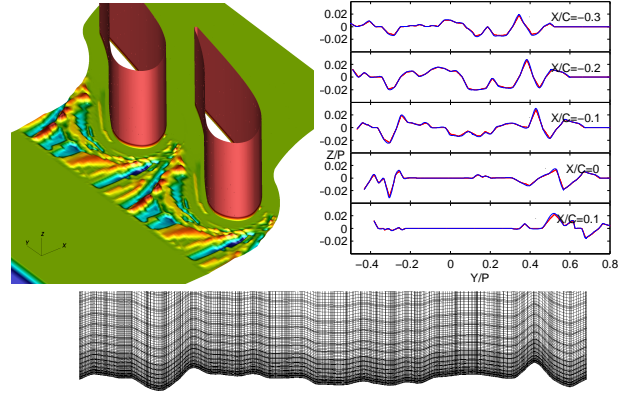

Fig. 5. The top left plot shows the contoured endwall surface, where the color shows surface elevation (red colored areas are higher than the smooth surface and blue colored areas lower). The contouring is applied from $X/C > -0.33$ to $X <\approx 40\% C_{ax}$ and across the entire span. The top right plot shows wall profiles at different X/C-locations, where the red line linearly connects only deformed mesh element edges. The blue line follows a spline interpolation between shifted spectral element corners in order to generate a smoother profile. The spline interpolated contour is used to generate the production mesh. The bottom plot shows a slice through the production grid at $X/C = -0.1$ with an aspect ratio of unity, across the entire pitch. Note that the periodic boundaries are only C0-continuous, not C1.

written out by the solver. The point elevation was then used to deform the spectral element mesh. In order to generate a smooth wall contour for the production runs, all spectral-element corner coordinates were extracted from the previous step, and a cubic spline interpolation was used to fit the data on a fine, regular grid ($\Delta X/P = \Delta Y/P = 0.02\%$); see Fig. 5, top right. The solver then deformed the GLL grid points on the wall by shifting them in the wall normal direction. All grid points located above, in the positive Z-direction and within the computational domain, were shifted in the same way but with linear decreasing magnitude; see Fig. 5, bottom. The deformation was applied between $X/C > -0.33$ and $X <\approx 40\% C_{ax}$, and across the entire pitch, with the exception of a circular nondeformed zone around the vane with a radius of $r/P = 0.05$ around the stagnation point. In the preprocessing steps, the endwall elevation was clipped to $\pm 5\%$ span. The intial condition for the numerical simulation of the contoured case was a certain time step of the smooth case, extrapolated on the deformed grid.

3 Results and discussions

In the following subsections, results of the main aspects of this study are discussed. The flow conditions upstream of the vane as generated by the novel inflow setup, heat transfer, and vortex dynamics as well as wall contouring based on the orthogonal expansion are presented.
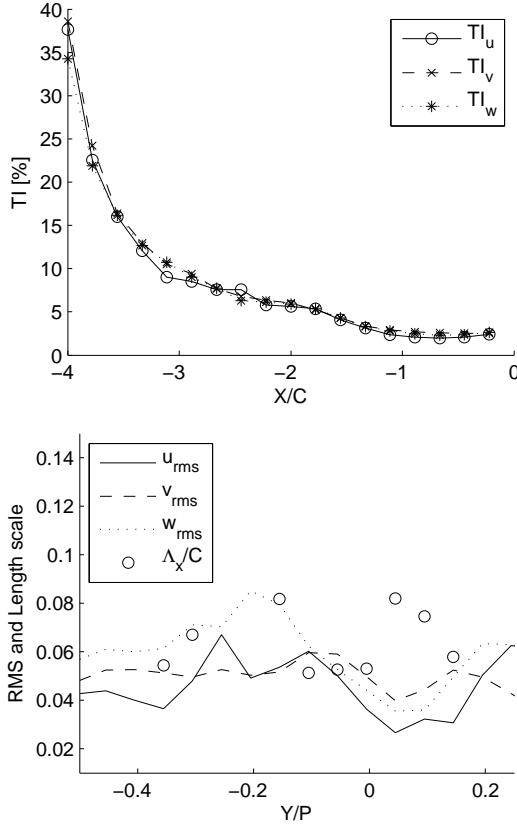
Fig. 6. The top plot shows the decay of turbulence intensity from the turbulence generating grid to the cascade leading edge ($X/C = 0$). The bottom plot shows the velocity RMS normalized with freestream velocity as well as normalized streamwise integral length scale across the pitch at a spanwise location of $Z/S = 0.25$ and $X/C = -1/3$.
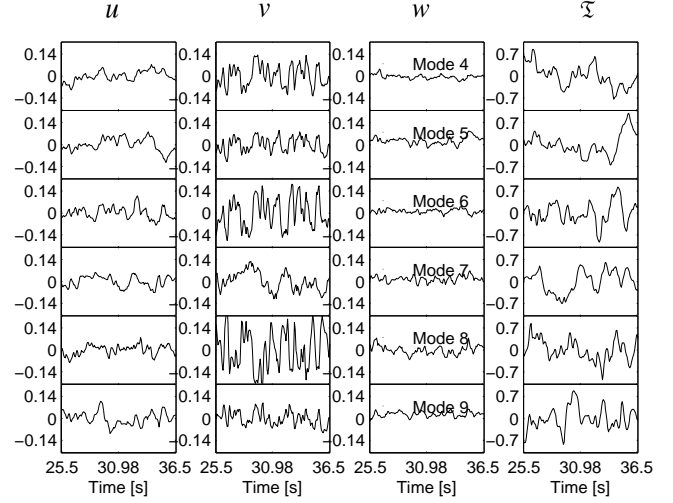

Fig. 7. The plots show the orthogonal time basis functions from an analysis covering the domain from $X/C = -1/3$ to the blade trailing edge as a function of flow time; u, v, w, and $\mathfrak{T}$ are the non-dimensionalized x, y, z-velocities and flow temperature. For better visualization, the modes are scaled. Modes 0 to 3 are not shown because they are constant over time and constitute the temporal average.
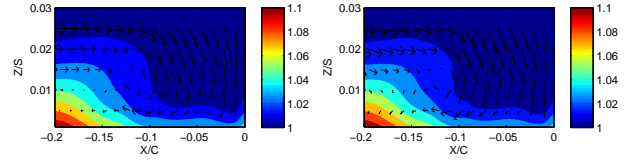

Fig. 8. The plots show the average in plane velocity vectors superimposed on a contour of fluid temperature normalized with inlet temperature on the stagnation plane. The data were derived from ensemble averaging all data samples (left) and a reduced order representation containing the sum of modes 0 to 3 (right).

3.1 Inflow characteristics

Since the blade geometry is a first-stage stator vane, the incoming flow should have a relatively large integral-length scale and turbulence intensity (Radomsky and Thole [4]). The inflow generation technique as described above is calibrated to match some of the parameters described therein and by Knost et al. [19]. While the boundary-layer displacement thickness compares favorably, the turbulence intensity (see Fig. 6, top) is closer to the lower one of the two cases examined experimentally. The integral length scale is lower as well. Upstream of the turbine cascade, the turbulent fluctuations are nearly isotropic. The turbulence intensity is around 2.1%, which is achieved by the vortex-containing inflow velocity field in combination with a forcing function acting against the dissipative terms of the momentum equation. The profiles in the pitchwise direction of those quantities are fairly homogeneous (see Fig. 6, bottom).

3.2 Orthogonal decomposition

To focus the orthogonal expansion on the stagnation and passage vortex, we consider only flow data between $X/C = -1/3$ and the blade trailing edge. Because of computer memory restrictions, the solution polynomial order for all orthogonal postprocessing was reduced from 7 to 5. The resulting time eigenfunctions are shown in Fig. 7. The first four modes (0 to 3) are not shown because they do not contain any time-varying parts but instead constitute the average for all signal components. No relation exists between mode number and signal component; thus, all four modes are needed in order to construct a complete average field. For validation purposes, Fig. 8 compares the average in-plane velocities in the stagnation plane superimposed on a contour of mean flow temperature derived from averaging all data samples (left) to the reduced order field containing the sum of modes 0 to 3 (right). The plots are almost identical, and slight deviations can be explained by the different grid resolution used for the full-scale simulation and the orthogonal decomposition postprocessing.

The different scales of temperature and velocity basis functions visible in Fig. 7 do not contain useful information and can be attributed to the signal nondimensionalizing and
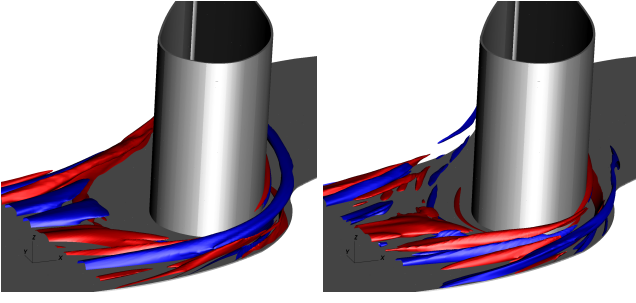
Fig. 9. The spatial eigenfunctions of mode 5 (left) and 6 (right) are plotted. A value of -2 was chosen for the blue isosurface and +2 for the red. Mode 5 was used for the subsequent wall contouring.
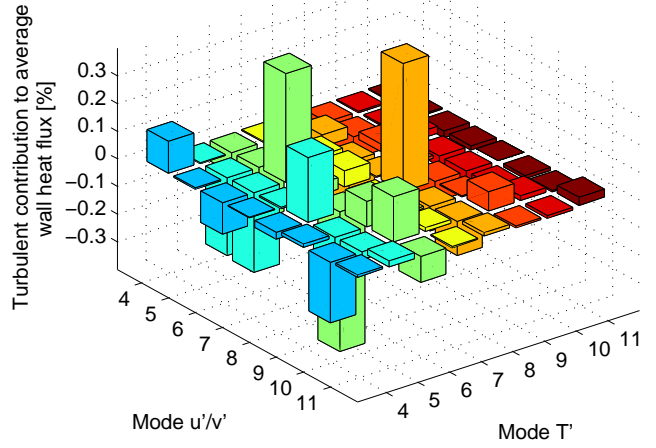

Fig. 10. The plot shows the contribution to wall heat flux for different mode combinations. The area of interest was defined from $X/C = -1/3$ to the vane front and from $Y/P = -0.4$ to $Y/P = 0.4$.

weighting. The dynamical information of each mode, however, can be analyzed: most notably, the pitchwise (y) component has higher fluctuating amplitudes than do the other three components. They are the highest in mode 8. Within the shown modes, the frequency of fluctuations is qualitatively the same. The temperature basis function of mode 5 has a fairly distinct, broad peak toward the end of the simulated time, which coincides with the time when the stagnation vortex core location is closest to the blade and most intense (the slightly longer one of the two blade approaching trajectories in Fig. 12, left). Thus, mode 5 shows the temperature impact for at least one of the two observed vortex trajectories. At the same time instant, the time function of that mode for the streamwise velocity has a fairly steep decrease. The spatial basis function of mode 5 is shown in Fig. 9, left. All spatial basis function contours are built by plotting isosurfaces at $\varphi^k(\vec{x}) = -2$ (blue) and $\varphi^k(\vec{x}) = 2$ (red), which is on average 15% of their maximum value. Mode 5 has the closest resemblance to the passage vortex. This mode, unlike the other high-energy ones, is not very active in the region of the horseshoe vortex.

In order to judge different modes' contribution to heat transfer in the stagnation area close to the vane, a single-mode heat transfer ranking was performed based on the presented time orthogonal basis set in the region from $X/C = -1/3$ to the vane front and from $Y/P = -0.4$ to $Y/P = 0.4$. The resulting matrix from evaluating Eq. (12) is shown in Fig. 10. Modes 6 and 8 have the highest positive contribution to turbulent wall heat flux, increasing heat transfer. The spatial basis function of mode 8 seems to capture the heat transfer dynamics in the region of high average Stanton number south of the stagnation point. The spatial eigenfunction of mode 6, depicted in Fig. 9, right, has one of the most distinctive regions of activity in the horseshoe vortex area among the high energy modes, but it is still relatively small compared with that of the structures in the mean flow. The peak in temperature basis function of mode 6 (at time 34.58 s) coincides with the highest gradient of horseshoe vortex core movement in the wall normal direction. This is the time when the leading-edge vortex upstream of the blade accelerates away from the wall into the free stream and gets advected toward the blade (compare Fig. 12, left). Mode 5 has

the highest contribution to lowering turbulent heat flux and was thus chosen for contouring the endwall.

3.3 Vortex dynamics

Velocity contour lines in combination with a velocity vector plot are shown in Fig. 11, left. Several leading-edge horseshoe vortices are identified, with the most intense one found nearest to the vane. The smaller ones are located further upstream and closer to the endwall. The main vortex is strong enough to accelerate freestream fluid toward the endwall, pushing it against the main flow. The incoming flow does not have enough momentum to suppress the formation of those secondary leading-edge vortices. These smaller vortices might not be as pronounced in the experimental results because of the much higher experimental Reynolds number. Compared with experiments, the vortex location in the lower Reynolds number numerical study is shifted farther upstream and closer to the endwall. The center of the strongest vortex does not coincide with the peak location of turbulent kinetic energy (Fig. 11, right); it is located farther downstream and away from the endwall compared with the mean vortex center. Compared with the experiments cited above, the peak location is shifted slightly farther upstream. The distance between the location of peak kinetic energy and mean vortex center is thus greater than in the higher Reynolds number experiments. The overall level of turbulent kinetic energy is about one-third of what is shown by Radomsky and Thole [4].

The high resolution of the simulation allows tracking the stagnation vortex core in space and time. The vortex center has been determined by computing the λ_2 vorticity domain-wide. The point where its magnitude is the highest on the stagnation plane and the corresponding vortex' spatial extent the largest, was tracked in space and time. From the time-resolved visualization, it is seen that the leading-edge
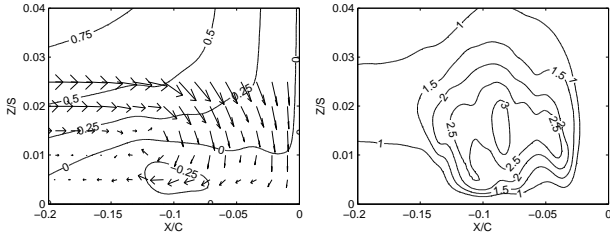
Fig. 11. The left plot shows contour lines of mean streamwise velocity and vectors of average in plane velocity components on the stagnation plane. Contours of turbulent kinetic energy, normalized by the freestream velocity squared and scaled by 100, are shown left. Data were taken on the stagnation plane.
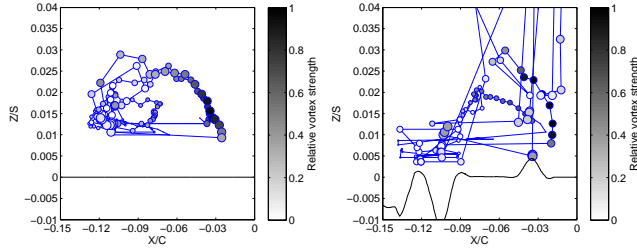

Fig. 12. The left plot shows the strongest stagnation vortex center's trajectory over time on the stagnation plane for the smooth case. The marker circle size changes with flow time (the bigger, the later in time is the point), whereas the color depicts the relative vortex strength (the darker, the lower the λ_2-value). The right plot shows the same for the contoured case.

vortices oscillate, vanish, and also merge. Sudden position changes in Fig. 12 result from one vortex vanishing while another has already formed at a different location. Once the new vortex is stronger, the tracking algorithm locks onto it. In Fig. 12, left, this can be seen at several time instants when the vortex core approaches the blade at $X/C = 0$. Because of the freestream momentum, the vortex is accelerated toward the vane stagnation; then it is pushed toward the endwall and vanishes. The core movement toward the blade is initiated by a movement away from the endwall; see Fig. 12, left. Two identical trajectories toward vortex destruction can be seen that form an upper bound to the core movement space. If those curves were completed to form a circle, the region of highest turbulent kinetic energy would roughly coincide with its center. The mean vortex position can be seen in Fig. 12, left, where the point density is the highest.

Figure 12, right, shows the same procedure applied to the contoured case. Note that high values of vorticity in the immediate near-wall region (up to approximately 0.3% span) were ignored because at the nonflat wall slopes, vorticity is high because of the boundary layer. The tracking algorithm would thus falsely ignore the (relatively weaker) freestream vortex cores and lock onto regions of high shear within the boundary layer. Comparing the contoured and smooth case, Fig. 12, left and right, one sees that the wall contour bump closest to the blade (at $X/C = -0.04$) is exactly located
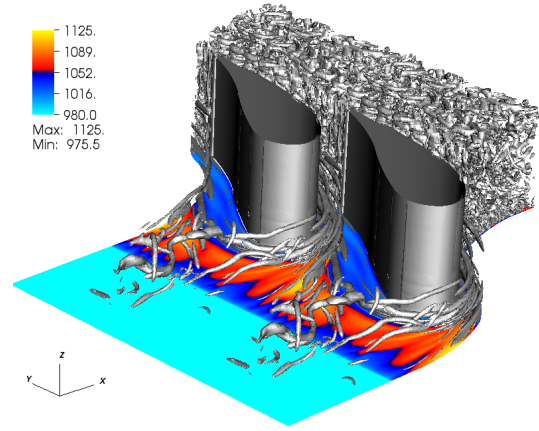

Fig. 13. The figure shows an isosurfaces of λ_2 vorticity (grey) and endwall temperature at one time instant. The computational domain has been copied once along the periodic direction for better visualization.

where the two blade-approaching vortex trajectories in the smooth case would hit the endwall if their pathways were extended. The contouring farther upstream is below the region where those trajectories originate. In the contoured case, at the same time instants the most intense vortices are found in the freestream flow. Since one can assume that the wall contouring does not alter the main flow, this means that the near-wall vortices are weaker than in the smooth case. Also, the vortex cores do not form as many connected trajectories as before. The two trajectories that show some similarity to the smooth case seem to rise and descend at a steeper angle and also travel along different paths toward the leading edge. The vortex formation zone at around $X/C = -0.12$ and $Z/S = 0.015$ observed in the smooth case (Fig. 12, left) is much less coherently populated, and its center has shifted toward the endwall. The wall contouring seems to have disrupted the horseshoe vortex movement and overall decreased its intensity.

3.4 Heat transfer

The impact of turbulent flow structures on endwall temperature is visualized in Fig. 13. The figure shows isosurfaces of coherent vorticity, visualizing multiple horseshoe vortices that merge while traveling through the passage. The wall temperature decreases below these structures as they are accelerating cooler freestream fluid toward the heated endwall. Upstream of the heated section, traces of freestream turbulent structures are visible. As seen in Fig. 6, the streamwise integral-length scale averaged over the simulation time varies between $0.05 < \Lambda_x/C < 0.08$. The relatively higher vorticity and qualitatively different flow structure downstream of the blade trailing edge visible in the figure motivated limiting the orthogonal decomposition to the passage only, since the horseshoe and passage vortex dynamics were the main interest in this study.

Examining heat transfer more closely in the stagnation area for the baseline case with the smooth wall, one can ob-
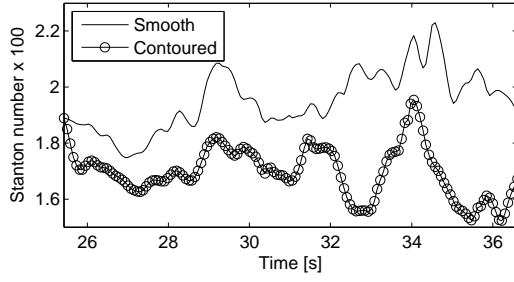
Fig. 14. The area-averaged Stanton number between $-0.15 < X/C < 0$ and $-0.1 < Y/P < 0.1$ for the smooth (solid line) and contoured (line with circles) case is shown as a function of simulation time. In the temporal average, the contoured endwall decreased the Stanton number by around 15%.
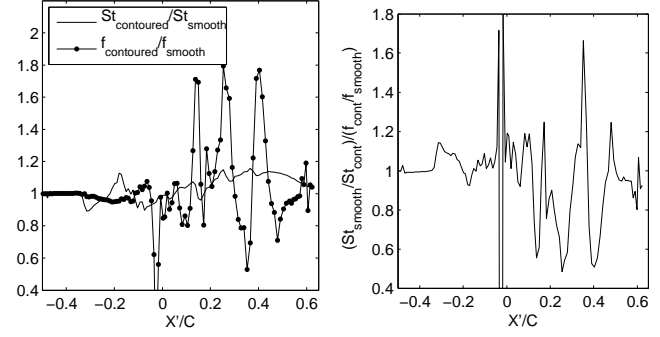

Fig. 16. The left plot shows the friction factor (circled line) and Stanton number (solid line) of contoured over baseline case integrated along the sample lines, where X' ist the coordinate along the passage connecting the sample line mid points. The right plot shows the fraction of Stanton numbers and friction factors such that an efficiency can be deduced.

serve fairly high fluctuations of surface heat transfer of about 20% (Fig. 14). The highest gradients in Stanton number (around 29 s and 34 s flow time) do not coincide in time with the two vortex trajectories with highest relative intensity as identified in Fig. 12, left. This situation might be due to the different areas under consideration: the Stanton number was derived from an endwall area average, whereas the vortex core tracing was performed on the stagnation plane. The spatial distribution of endwall heat transfer in terms of Stanton number of the smooth case shows the highest values slightly south of the stagnation point and in the wake of the blade. Induced by the passage vortex, there is a deflection of a high heat transfer zone within the passage toward the suction side. Compared with the cited experiments, the computational heat transfer values are higher upstream of the vane but roughly the same in the blade wake. These deviations are expected because of the experimental Reynolds number was much higher.

In order to judge the efficiency and effectiveness of endwall contouring along the passage, time-averaged static wall temperature and time-averaged static wall pressure were evaluated on sample lines placed in such a way that they follow the blade curvature; see Fig. 15. The time-averaged results were first extrapolated onto a smooth, regular grid from which line data were interpolated. Then, the values were integrated along the lines; 110 sample lines cover the heated and deformed section up to the blade trailing edge. In Fig. 15, the underlying color contour depicts the mean static wall temperature for the contoured case. The dark blue regions where the blades are located are not part of the original domain and are not used for postprocessing. The computational domain with periodic boundaries in the pitchwise direction extended from $Y/P = 0.5$ to $Y/P = 1.5$.

Figure 16, left, shows the time-averaged Stanton number and friction factor fractions of the smooth over the contoured case as a function of position within the passage. The friction factor is based on the wall static pressure plus the dynamic pressure varying with the passage width. The reference pressure and flowrate were taken as an area average close to the domain inlet ($X/C = -4.6$), with the outflow through the suction slot accounted for as well. For computing the Stan-

ton number, a reference temperature was computed based on X', the location in the passage, and the thermal energy put in up to that point via endwall heating. The plots represent integral values from the reference location to X'. As expected, there is no change between the smooth and contoured case up to the start of the wall contour at $X/C > -0.33$. Approaching the blade, both the Stanton number and friction factor are reduced, where the Stanton number shows a single peak at $X/C - 0.2$. This is the location where the endwall contour has a relatively high bump (compare with Fig. 5, top right, at $-0.2 < X/C < -0.1$ and $Y/P = 0.4$) and thus generates a larger area of attack for the free stream to disrupt the thermal boundary layer. Along the passage, the Stanton number is higher in the contoured case, which is undesired because the endwall is intended to stay cool. The downward peak in friction factor augmentation close to the blade is likely due to increased wall static pressure in the stagnation area, where static wall pressure is not a good indicator of passage pressure drop. Within the passage itself, the friction factor changes to almost 1.8 times its baseline value, which might also be explained by the increased dynamics within the passage flow structures because of the wall contour. Nonetheless, when getting close to the trailing edge, the friction factor seems to drop down toward the baseline value again. An efficiency of the endwall contouring is shown in Fig. 16, right. The Stanton number augmentation is related to the friction factor change from the smooth to the contoured case. We note that a decrease in Stanton number ($St_{smooth}/St_{cont} > 1$, yielding less heat exchange with the surface) was deemed beneficial to efficiency when accompanied by a decrease in friction factor $f_{cont}/f_{smooth} < 1$. In the stagnation region, the decrease in Stanton number has not led to a significant increase in friction; the efficiency is above 1 for the most part (the only exception being the single bump mentioned above). Within the passage, both heat transfer and pressure drop are higher than in the smooth case. The endwall deformation, however, is limited to roughly $X'/C < 0.5$ because the stagnation area was the focus of this study. As
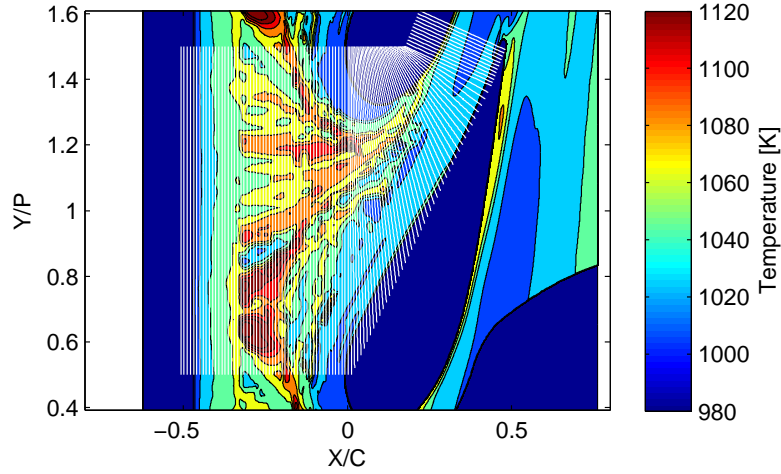
Fig. 15. For postprocessing heat transfer and pressure drop along the passage, data were interpolated on 110 sample lines (white). The underlying color contour depicts the time-averaged temperature on the endwall of the contoured case. Note that the vane bodies, which are not part of the mesh, are colored blue. Upstream of the passage, the lines span the entire computational domain, extending from $Y/P = 0.5$ to $Y/P = 1.5$. In the figure, the domain has been copied along the periodic direction for better visualization.

in Fig. 16, left, the erratic behavior of friction factor change dominates and is much higher than the change in heat transfer. As the trailing edge is approached, the augmentation is less erratic but harmful to pressure drop and heat transfer at the same time.

Another aspect critical to the durability of machine parts manufactured from metal is the temperature fluctuation induced by the flow. Figure 17 shows the temperature RMS at the wall from the contoured and smooth case. Most notably, there is a region of high dynamics (as well as high surface temperature, which in turn means good cooling) upstream of the stagnation point. The wall contour at this point consists of trenches such that protective low-momentum fluid accumulates without extensively mixing with the mean flow. The bump mentioned above appears as a dark strip in the mean wall temperature plot, top right, slightly above the zone of minimal heat exchange. The contours of time-averaged temperature, top plots, show an uneven distribution of the improvements achieved by the wall contour. For example, a small region winding along the blade pressure side seems to show higher heat transfer, whereas the region upstream of the zone where the vortex is active experiences a higher wall temperature or less heat exchange. The simulation did not include a conducting wall. Thus, the relatively high gradients and dynamics are likely to be smoothened when a conducting layer of finite thickness is included in the computational domain.

4 Conclusions

A direct numerical simulation of a first stage-stator blade with less-than-engine-condition Re = 10,000 was performed. The high-intensity, high-length-scale combustor exit flow was modeled with a vorticity containing inflow and geometric mesh features, with which a turbulence freestream
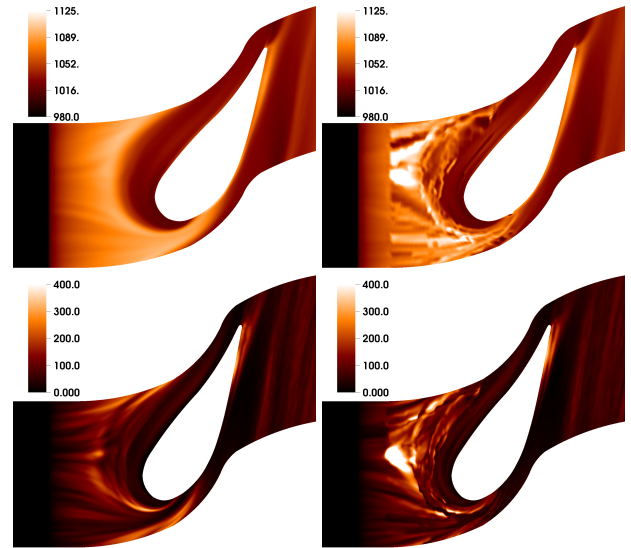

Fig. 17. The plots show average wall temperature of the smooth case (top left) and the contoured case (top right) as well as RMS of wall temperature of the contoured case (bottom right) and smooth case (bottom left).

intensity of close to 3% and a streamwise length scale of around 0.08 C could be achieved. The leading-edge horseshoe vortex appears to be not one single structure but, instead, multiple ones that move, vanish, and merge. The dynamics of the strongest leading-edge horseshoe vortex were observed with a core-tracking algorithm applied on the stagnation plane. This showed that the vortex has the tendency to travel away from the endwall toward the blade, where it then gets pushed back down and vanishes. Two almost-identical core trajectories along this path were observed. An orthogonal decomposition based on time was performed on the flow

data. In order to reconstruct an averaged field, the first four modes need to be used. Their time functions are constant. The time instant of the largest and broadest peak in the temperature and streamwise velocity time basis function of mode 5 is identical to the time when the vortex is closest to the blade. The spatial eigenfunction of this mode represents the passage vortex and is not active in the horseshoe vortex region. This mode is, however, the biggest contributor to lowering turbulent heat transfer in a control plane upstream of the leading edge. The highest contribution to increasing heat transfer is made by modes 6 and 8. Two peaks in their time basis function coincide with the time instant when the gradient in vortex core wall normal velocity is highest. The spatial basis function of mode 6 shows the most distinct imprint of the horseshoe vortex, though it is relatively small compared with the freestream structures. Modes 6 and 8 also have the highest fluctuations in the pitchwise velocity component. No mode could be found within the first 10 that resembles only or mainly the leading-edge horseshoe vortex. Contouring the endwall by POD-based analysis yielded a lower Stanton number in the stagnation area for only a slight increase in friction factor.

References

[1] Gaugler, R. E., and Russell, L. M., 1984, "Comparison of visualized turbine endwall secondary flows and measured heat transfer patterns," *ASME J. Eng. Gas Turbine Power,* **106**, pp. 168–172.

[2] Kang, M., Kohli, A., and Thole, K. A., 1999, "Heat transfer and flowfield measurements in the leading edge region of a stator vane endwall," *J. Turbomachinery,* **121**, pp. 558–568.

[3] Devenport, W. J., and Simpson, R. L., 1990, "Time-dependent and time-averaged turbulence structure near the nose of a wing-body junction," *J. Fluid Mechanics,* **210**, pp. 23–55.

[4] Radomsky, R., and Thole, K. A., 2000, "High freestream turbulence effects in the endwall leading edge region," *J. Turbomachinery,* **122**, pp. 699–708.

[5] Gregory-Smith, D. G., and Cleak, J. G. E., 1992, "Secondary flow measurements in a turbine cascade with high inlet turbulence," *J. Turbomachinery,* **114**, pp. 173–183.

[6] Spencer, M. C., Jones, T. V., and Lock, G. D., 1996, "Endwall heat transfer measurements in an annular cascade of nozzle guide vanes at engine representative Reynolds and Mach numbers," *Int. J. Heat and Fluid Flow,* **17**, pp. 139–147.

[7] Langston, L. S., 2001, "Secondary flows in axial turbines - a review," *Ann. New York Acad. Sci.,* **934**, pp. 11–26.

[8] Thole, K., 2008, personal communication.

[9] Sadiki, A., Klein, M., and Janicka, J., 2003, "A digital filter based generation of inflow data for spatially developing direct numerical or large eddy simulations," *J. Computational Physics,* **86**, pp. 652–665.

[10] Jacobs, R. G., and Durbin, P. A., 2001, "Simulations of bypass transition," *J. Fluid Mechanics,* **428**, pp. 185–212.

[11] Ball, K. S., Sirovich, L., and Keefe, L. R., 1991, "Dynamical eigenfunction decomposition of turbulent channel flow," *Int. J. Num. Meth. Fluids,* **12**, p. 587.

[12] Duggleby, A., Ball, K., and Schwänen, M., 2009, "Structure and dynamics of low Reynolds number turbulent pipe flow," *Phil. Trans. Roy. Soc. A,* **367**(1888), pp. 473–488.

[13] Aubry, N., Guyonnet, R., and Lima, R., 1991, "Spatiotemporal analysis of complex signals: Theory and applications," *J. Statistical Physics,* **64**, pp. 683–739.

[14] Handler, R. A., Housiadas, K. D., and Beris, A. N., 2006, "Karhunen-Loève representations of turbulent channel flows using the method of snapshots," *Int. J. Num. Meth. Fluids,* **52**, pp. 1339–1360.

[15] Fischer, P., Lottes, J., Kerkemeier, S., Obabko, A., and Helsey, K., 2008, nek5000 Web page, http://nek5000.mcs.anl.gov.

[16] Lottes, J. W., and Fischer, P. F., 2004, "Hybrid multigrid/Schwarz algorithms for the spectral element method," *J. Sci. Comp.,* **24**(1), pp. 45–78.

[17] Walsh, O., 1992, "Eddy solutions of the Navier-Stokes equations," *The Navier-Stokes Equations II - Theory and Numerical Methods*, Vol. 1530 of *Lecture Notes in Mathematics*. Springer-Verlag, Heidelberg, Germany, pp. 306–309.

[18] Kays, W., and Crawford, M., 1980, *Convective Heat and Mass Transfer,* McGraw-Hill, New York.

[19] Knost, D. G., Thole, K. A., and Duggleby, A., 2009, "Evaluating a slot design for the combustor-turbine interface," ASME paper GT-2009-60168.